Chinese Chemical Letters 37 (2026) 111439

Contents lists available at ScienceDirect

Chinese Chemical Letters

journal homepage: www.elsevier.com/locate/cclet

Efficient electrochemical bromine extraction from low-concentration brine *via* a flow electrolyzer

Ziyu Zhao[a], Tianyue Qian[a,*], Changyu Yan[a], Xinhua He[a], Zhou Xu[a], Wenjing Li[a], Zhiling Xin[b,*], Huifang Zhang[c,*], Xuefeng Qian[a], Jiantao Zai[a,*]

[a] *Shanghai Electrochemical Energy Devices Research Centre, School of Chemistry and Chemical Engineering, Shanghai Jiao Tong University Shanghai 200240, China*

[b] *Shanghai Key Laboratory of Materials Protection and Advanced Materials in Electric Power, Shanghai University of Electric Power, Shanghai 200090, China*

[c] *Key Laboratory of Green and High-end Utilization of Salt Lake Resources, Qinghai Institute of Salt Lakes, Chinese Academy of Sciences, Xining 810008, China*

ARTICLE INFO

Article history:
Received 12 April 2025
Revised 4 June 2025
Accepted 10 June 2025
Available online 10 June 2025

Keywords:
Hydrogen-bromine flow cell
CO_2 activation
Bromine extraction
Low-concentration brine
Electrochemical oxidation

ABSTRACT

Bromine, a vital industrial chemical raw material with extensive applications, faces extraction challenges from diluted underground brine due to high energy consumption and low efficiency in conventional methods. In this study, we introduce a CO_2 activation of acid-thermal treated graphite felt (AHGF-Y) as a highly effective negative electrode for bromine extraction, achieving remarkable efficiency exceeding 90%. With enriched oxygen-containing functional groups introduced by CO_2 activation serving as active sites, the engineered bromine extraction electrodes demonstrates superior bromine oxidation reaction (BrOR) under high Cl/Br ratio conditions. Coupled with hydrogen production, in electrolyte with a Cl/Br ratio of 38, AHGF-Y operated at a low overpotential and achieved remarkable bromine extraction efficiency (94%), with minimal energy consumption (1.61 kJ/g). Notably, when applied to underground brine with high Cl/Br ratio of 255 and multiple interfering ions, AHGF-Y maintained extraction efficiency of 95.5%, significantly outperforming other reported works. Furthermore, AHGF-Y achieved an near-unity Faradaic efficiency (F.E.) of up to 99.7% in a scale-up hydrogen-bromine flow cell (HBFC), enabling simultaneous bromine extraction and hydrogen production. These results highlighted the potential of AHGF-Y as a sustainable and efficient material for large-scale bromine extraction from underground brine.

© 2026 Published by Elsevier B.V. on behalf of Chinese Chemical Society and Institute of Materia Medica, Chinese Academy of Medical Sciences.

As a crucial and irreplaceable chemical precursor, bromine serves as a key chemical raw material widely utilized in the synthesis of industrial products such as retention agents, fire extinguishing agents, and flame retardants [1–3]. However, its supply chain faces growing challenges due to surging global demand. The main bromine sources include underground brine, salt lake brine, seawater, intermediate brine from the salt production process, and mother liquor after salt production [4–10]. The conventional air blow-out method, utilizing Cl_2 as an oxidant, operates effectively in bromine extraction within the bromine concentration range of 200–400 mg/L, but poroves insufficient for diluted sources (<120 mg/L) such as underground brines or seawater [4].

Therefore, there is an urgent need to develop alternative methods for bromine extraction. Compared to chemical oxidation, electrochemical oxidation has been attracting increasing attentions in the field of bromine extraction due to its excellent selectivity, simplified production process, clean production, and low energy consumption [11]. Zhou *et al.* enhanced extraction efficiency from 25.4% to 77.8% by optimizing the electrode area, yet the electrochemical oxidation process remains energy-intensive, potentially limiting cost-effectiveness for large-scale applications and generating by-products like chloride compounds [8]. Cohen *et al.* further reduced energy consumption by lowering it to 2.24 kJ/g using activated carbon cloth [2]. Nonetheless, this approach resulted in a limited bromine extraction yield of 1.4%. To address both energy and yield issues, Sun *et al.* achieved a Faraday efficiency (F.E.) of 60% to 90% and an energy consumption of 6 kJ/g in oil and gas wastewater using a graphite electrode at a Cl/Br ratio of 43 [15]. Despite the efforts to improve electrochemical bromine extraction in recent studies, critical challenges persist in high energy consumption, limited bromine extraction yield, and poor applicability in low bromine concentration and high Cl/Br ratios systems, hindering their practical scalability and application potential.

* Corresponding authors.
E-mail addresses: qiantianyue@sjtu.edu.cn (T. Qian), xinzhiling@126.com (Z. Xin), zhanghf@isl.ac.cn (H. Zhang), zaijiantao@sjtu.edu.cn (J. Zai).

https://doi.org/10.1016/j.cclet.2025.111439
1001-8417/© 2026 Published by Elsevier B.V. on behalf of Chinese Chemical Society and Institute of Materia Medica, Chinese Academy of Medical Sciences.

Additionally, in practical production, the Br^- extraction process is further complicated by competitive Cl^- interference, making the Cl/Br ratio a critical factor to consider in the bromine extraction process [2,12–14]. The principle of electrochemical oxidation is based on the difference in standard oxidation potentials between bromide ions (Br^-) and chloride ions (Cl^-): The Br_2/Br^- couple has a standard oxidation potential of 1.087 V, which is lower than that of the Cl_2/Cl^- couple at 1.358 V [6]. This narrow potential window demands electrocatalytic materials with enhanced selective oxidation activity for bromine, yet effective catalysts for high-selectivity bromine extraction at high Cl/Br ratios remain lacking. To address the challenges of high Cl/Br ratios, carbon-based materials such as graphite felt (GF) have been widely studied due to their excellent conductivity. Modifying GF through oxygen or metal doping has shown potential to enhance bromine adsorption and redox kinetics [15–20]. For instance, platinum supported on carbon materials exhibits excellent electrochemical performance in electrooxidation reactions; however, its high cost and limited stability constrain its application as an electrode material [23]. Thus, the long-term stability and selective oxidation of bromine on carbon electrodes prepared using these conventional methods remain a significant challenge [21–24].

To address these challenges, including high energy consumption, low extraction yield, and poor selectivity in high Cl/Br ratio solutions, we employed CO_2 activation of acid-thermal treated graphite felt (AHGF-Y) to enhance selectivity and reduce the overpotential of the BrOR electrode. Also, a highly efficient hydrogen-bromine flow cell (HBFC) system is designed to overcome the mass diffusion limitation in conventional static electrochemical cells. Under flow conditions 1 g/L Br^-, and 17 g/L Cl^-, AHGF-Y achieved bromine extraction yield of nearly 94 % and energy consumption of just 1.61 kJ/g. Even in underground brine containing interfering ions (such as SO_4^{2-} and NO_3^-) with extremely low bromine concentration (0.15 g/L Br^-) and high chloride content (17 g/L Cl^-), the system maintained exceptional extraction efficiency of 95.5 %, demonstrating its practical potential for low-grade bromine extraction. Moreover, when applied to HBFC for scale-up testing, F.E. of up to 99.7 % was achieved. Finally, hydrogen was co-produced at the positive electrode, consistent with the theoretical hydrogen yield. Our results demonstrate that AHGF-Y-based technologies can achieve efficient, economical, and environmentally friendly co-production of bromine and hydrogen. In the future, these technologies are expected to be scaled up for industrial applications, providing robust support for the integration of renewable energy and the development of green chemical processes.

Materials: The graphite felt (GF, thickness: 3 mm) was obtained from Hebei King Carbon Technology Co., Ltd. Sodium bromide (AR), sodium chloride (AR), sodium sulfate (AR), and sulfuric acid (AR) were purchased from Sinopharm Chemical Reagent Co., Ltd. All chemicals and solvents were used without further purification.

The GF was immersed in a 6 mol/L sulfuric acid solution for 12 h, rinsed with deionized water until neutral pH, and then dried in a vacuum oven, resulting in acid-modified graphite felt (AGF). It was then calcined in a muffle furnace at 300 °C for 2 h to obtain acid-heat-treated graphite felt (AHGF).

A single-zone horizontal tube furnace was flushed for at least 30 min before heating. The sample was heated under a CO_2 atmosphere at a rate of 10 °C/min to 850 °C and maintained at 850 °C for X h (X = 0.5, 0.75, 1, 1.5, 2, 2.5). During the heating process, the gas flow rate was set to 200 mL/min to ensure an adequate CO_2 supply. After the designated heating period, the sample was cooled under a nitrogen flow of 200 mL/min to obtain AHGF-Y, where Y = 10X.

A platinum-loaded AHGF (Pt-AHGF) was left to stand at a temperature of 30 °C in 30 mL solution of chloroplatinic acid for 1 h, and then activated under H_2/Ar at 400 °C for 5 h.

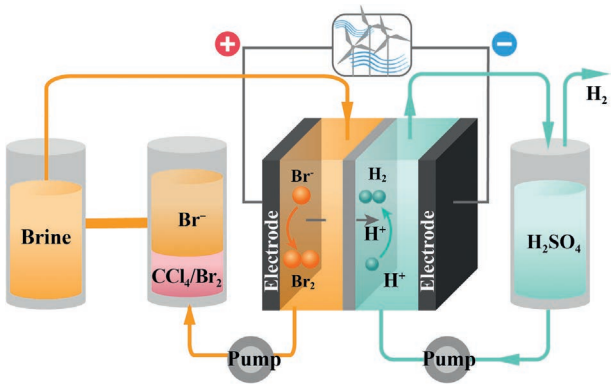


Fig. 1. Diagram of hydrogen-bromine flow cell.

Nitrogen (N_2) adsorption and desorption isotherms (BSD-660 M (A6B3M), China) were used to classify pore structures and perform physical characterization, with temperature control maintained at low temperature by liquid nitrogen (77 K). The specific surface area was determined using the Brunauer–Emmett–Teller (BET) method. The pore size distribution was calculated from the adsorption branch using the non-local density functional theory (NLDFT) method. The morphology and surface chemical differences of the AHGF samples were determined using a scanning electron microscope (SEM, Nova Nano SEM 230, USA). Surface properties and elemental analysis were conducted using energy-dispersive spectroscopy (EDS) elemental mapping to analyze the surface characteristics and element distribution on the AHGF electrodes. The contact angles of the samples were measured using an optical contact angle measuring device (DSA30, Germany). The concentration of bromide ions (IC) was measured using ion chromatography (IC, ICS5000+, Thermo Fisher). The electronic states of elements on the AHGF electrode surface were analyzed by X-ray photoelectron spectroscopy (XPS, Thermo Fisher Scientific, USA). The structural characteristics of the electrodes were analyzed using an X-ray diffractometer (XRD, Miniflex 600-C, Japan). The I_D/I_G ratio of the graphite felt electrodes was analyzed by Raman spectroscopy (Raman, Thermo Fisher Scientific, USA). The graphite felt samples were characterized using a Fourier transform infrared spectrometer (FT-IR, Thermo Fisher, USA) to investigate changes in their surface functional groups.

The study of electrode performance, a 0.2 mol/L NaBr solution was used as the standard electrolyte in single-cell three-electrode electrochemical experiments. Linear sweep voltammetry (LSV), cyclic voltammetry (CV), and Tafel slope measurements for electrocatalytic performance were all implemented in a three-electrode system on the CHI760E electrochemical workstation (CH Instruments, USA). A saturated calomel electrode (SCE, from Shanghai CH Instrument Ltd.) and a platinum electrode (1 cm × 1 cm, from Gaoss Union (Tianjin) Photoelectric Technology Ltd.) were used as the reference and counter electrodes, respectively. Electrochemical impedance spectroscopy (EIS) at open circuit potential (OCP) and *in-situ* EIS were performed within the frequency range from 1 MHz to 0.1 Hz on the Zahner Zennium electrochemical workstation (Zahner, Germany). To measure the electrode capacitance using cyclic voltammetry, a 0.1 mol/L Na_2SO_4 solution was used. All chemicals were used as received without further purification. The following equation was used to convert the potentials to the SHE scale:

$$E(vs.\ SHE) = E(vs.\ SCE) + 0.244V \quad (1)$$

The construction diagram of the internal flow cell structure can be found in Fig. 1 (FRS-GR-1.6, from Taizhou TiSing Electrochemisry Co., Ltd.). As shown in Fig. S1 (Supporting information), the flow

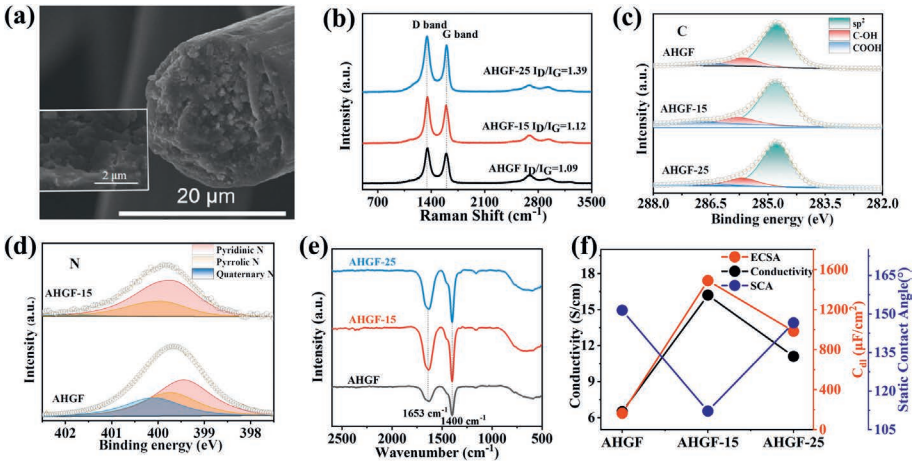


Fig. 2. (a) SEM images of AHGF-15. (b) Raman spectra of AHGF and AHGF-Y. (c) XPS spectra of C 1s. (d) XPS spectra of N 1s. (e) FTIR spectra of AHGF and AHGF-Y. (f) ECSA, conductivity, SCA curves of AHGF and AHGF-Y.

path design features a diagonal interleaving channel (integrated graphite flow field plate). The electrodes in the flow cell are installed in an embedded configuration.

The underground brine is first extracted using CCl_4 to remove most of the organic substances, and the negative electrolyte measured by ion chromatography is expressed as 0.15 g/L Br^-, 17.0 g/L Cl^-, 0.044 g/L SO_4^{2-} and 0.027 g/L NO_3^-. Based on this composition, we prepared anion solutions with Cl^- concentration of approximately 17 g/L and Br^- concentrations of 1, 0.68, and 0.12 g/L.

The device of HBFC, illustrated in Fig. 1, was conducted at room temperature (25±3 °C) in a sealed flow cell to achieve selective oxidation of bromide ions. The positive electrode and the sealed negative electrode chamber were separated by a cation exchange membrane (Nafion 117, Sigma-Aldrich). On one side of the negative electrolyte side, two containers each contained 40 mL of negative electrolyte solutions, while another container held 20 mL of negative electrolyte and 20 mL of CCl_4. The electrolyte was thoroughly mixed and circulated for bromine extraction using a flow pump. In non-cyclic tests, the bromine-extracted solution did not return to the negative electrode chamber for repeated extraction.

AHGF and AHGF-Y were used as the negative electrode, installed in an embedded configuration. Pt-AHGF electrode served as the positive electrode. The bromine extraction experiments were conducted in constant current mode. Unless otherwise specified, the bromine extraction current at the negative electrode was set to 15 mA, and controlled using a DH7000C electrochemical workstation from Jiangsu Donghua Analytical Instrment Co., Ltd.

The bromine generated during oxidation was directly introduced into a beaker containing carbon tetrachloride for subsequent quantification *via* ion chromatography. Meanwhile, in the positive electrode chamber, protons gained electrons on the surface of the Pt-AHGF electrode to generate hydrogen gas.

X-ray diffraction (XRD) analysis was used to confirm whether CO_2 activation altered the crystal structure of the AHGF material. In the XRD patterns (Fig. S2 in Supporting information), the phase compositions of the three samples are similar, and the crystal structure of AHGF after CO_2 activation shows no significant change. The broad peak observed at $2\theta = 25.0°$ is a typical characteristic of graphite felt [25]. This indicates that the crystal structure of graphite felt is not affected by CO_2 activation.

The individual fibers of AHGF and AHGF-Y are shown in Fig. S3 (Supporting information) and Fig. 2a. The chemical composition of the AHGF-15 sample was analyzed using the SEM-EDS method in Fig. S4 (Supporting information). The samples were primarily composed of carbon. The formation of surface micropores and defects is associated with the Boudouard Reaction ($C + CO_2 \rightarrow 2CO$) occurring on the AHGF surface during activation. As shown in Fig. 2a, the SEM images reveal that after CO_2 activation, the carbon structure develops an irregular pore morphology. The surface roughness of AHGF-Y increases significantly, and small defects are introduced on the carbon fiber surfaces due to CO_2 activation.

Table 1
Distribution of carbon functional groups in AHGF and AHGF-Y.

Sample	sp^2	C–OH	C=O	Functional group (C–OH, C=O)
AHGF	0.81	0.05	0.14	0.19
AHGF-15	0.73	0.19	0.09	0.27
AHGF-25	0.83	0.12	0.05	0.17

To confirm the carbon bonding states in the AHGF and AHGF-Y materials, Raman spectroscopy was conducted. The D-band peak typically appears at around 1350 cm^{-1}, while the G-band peak is located at approximately 1580 cm^{-1} [26]. The intensity ratio of the D-band to the G-band (I_D/I_G) reveals the degree of disorder in the carbon structure. As shown in Fig. 2b, the I_D/I_G ratio for AHGF-15 is 1.12, indicating a higher degree of structural disorder compared to AHGF ($I_D/I_G = 1.09$) and AHGF-25 ($I_D/I_G = 1.39$). The increased disorder is likely caused by the introduction of additional defects in the carbon structure during the CO_2 activation stage, which reduces crystallinity. The lower degree of graphitization in AHGF-15 leads to the formation of more surface active sites, pores, and defects. These defects and active sites enhance Br^- adsorption.

XPS analysis was used to confirm the types of carbon and nitrogen elements in the AHGF and AHGF-Y electrodes. The C 1s spectra in Fig. 2c were deconvoluted for AHGF, AHGF-15, and AHGF-25 to investigate the effects of CO_2 modification on the surface functional groups of graphite felt. The results show that the peak for sp^2 hybridized carbon appeared at 284.8 eV, hydroxyl carbon at 286.0 eV, and carbonyl carbon at 286.7 eV [27–29]. As indicated in Table 1, the functional group content (C–OH, C=O) in AHGF-15 reached 27 %, superior to that in AHGF and AHGF-25, respectively. The presence of these functional groups affects the electronic structure of the GF, which may alter the surface activity, further influencing the charge transfer efficiency in electrochemical reactions and impacting bromine extraction capability. CO_2 activation introduced oxygen functional groups (C–OH, C=O), serving as active sites to enhance catalytic efficiency in electrochemical reactions.

Table 2
Distribution of nitrogen functional groups in AHGF and AHGF-Y.

Sample	Quaternary N	Pyrrolic N	Pyridinic N
AHGF	0.23	0.30	0.46
AHGF-15	0.02	0.18	0.79

Research has shown through XPS analysis that nitrogen-doped carbon materials provide bromine adsorption sites, with nitrogen functional groups undergoing chemical reactions with Br_2/Br^- [28]. The N 1s XPS spectra (Fig. 2d) were deconvoluted into four different nitrogen functional groups: pyridinic nitrogen (399.4 eV), pyrrolic nitrogen (400.1 eV), and quaternary ammonium nitrogen (401.0 eV) [30]. The atomic content of the nitrogen functional groups is summarized in Table 2. Pyridinic nitrogen could significantly enhance bromine extraction yield by promoting bromide ion adsorption, facilitating electron transfer, improving adsorption properties, and stabilizing intermediates [28]. In contrast, the positive charge of quaternary ammonium nitrogen would hinder bromine extraction by stabilizing negatively charged intermediates and generating steric hindrance, which suppressed active sites and electron conduction. According to Table 2, it can be concluded that AHGF-15 has a high pyridinic nitrogen content of 79 % and nearly zero quaternary ammonium nitrogen.

The FTIR spectrum in Fig. 2e showed that the peaks at 1653 and 1400 cm^{-1} were attributed to the stretching vibration of the carbonyl group (C=O) and the bending vibration of the –OH group, respectively. In the AHGF-Y samples, the peak intensities of C=O and –OH changed under different treatment conditions. The result indicated that CO_2 activation increased the content of –OH and C=O functional groups, which was also consistent with the XPS results. This further demonstrated the successful construction of AHGF-Y enriched with COH and C=O functional groups.

The static contact angle (SCA) was used as an indicator to characterize changes in the hydrophilicity of electrode materials. As shown in Fig. 2f and Fig. S5 (Supporting information), the SCA of AHGF-15 was 112.2°, smaller than that of AHGF, indicating that AHGF-15 had better hydrophilicity due to the presence of more oxygen-containing functional groups on its surface. It has been reported that porous carbon materials rich in oxygen and nitrogen exhibit better wettability and enhanced affinity with aqueous electrolytes compared to other pretreatment methods [31–36]. In this work, AHGF-15 formed a structurally stable porous carbon layer rich in oxygen and nitrogen functional groups. This improved negative electrode not only enhanced the hydrophilicity of the AHGF-15 electrode but also improved the redox kinetics of bromine. Relatively better electrolyte wettability promotes ion transport, thereby increasing the electrochemical reaction rate and overall bromine extraction yield. In the case of AHGF electrodes without CO_2 activation, it was observed that relatively hydrophobic electrodes failed to absorb the electrolyte, resulting in minimal participation of the electrode in the bromine redox reaction. As shown in Fig. 2f, AHGF-15 exhibits the highest conductivity, which might be attributed to the presence of appropriate defects or vacancies that could tune the band gap structure and enhance electron mobility. The introduction of nitrogen could increase the electron density of the carbon material, thereby improving its conductivity.

To further investigate the active sites of AHGF and AHGF-Y, the electrochemically active surface area (ECSA) was tested at different scan rates (10–30 mV/s) (Fig. 2f and Fig. S6 in Supporting information). The electrochemical response of AHGF is primarily attributed to the contribution of the electrochemical double-layer capacitors (EDLCs), as indicated by the ideal polarization characteristics, compared to AHGF-Y in Fig. S6 [37,38]. Despite the advantages of EDLCs, such as fast adsorption and ion exchange, they

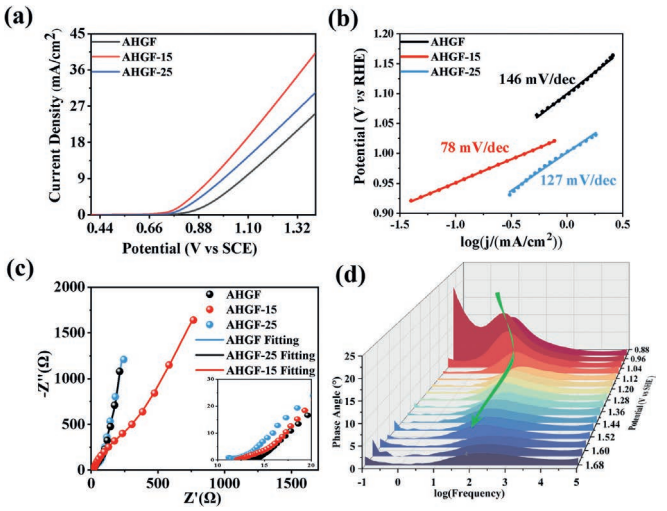


Fig. 3. (a) The LSV curves of AHGF and AHGF-Y electrodes. Scan rate of 100 mV/s, range from 0.4 V to 1.4 V. (b) Tafel Curves of AHGF and AHGF-Y. (c) The EIS diagram in 0.2 mol/L NaBr solution of AHGF and of AHGF-Y. (d) *In-situ* EIS diagram of AHGF-15.

store energy only through physical adsorption, lacking active sites that participate in complex electrochemical reactions [39,40]. As a result, EDLCs perform poorly in handling bromine evolution reactions, which also explains why the efficiency of AHGF in the bromine extraction process is almost zero. In contrast, AHGF-Y showed a higher resistive behavior, and the resistive features in the ECSA curves were due to the diffusion constraints of the electrolyte within the pores [37,38]. To further compare and evaluate ECSA of several materials, their double-layer capacitance (C_{dl}) was measured using CV in a 0.1 mol/L Na_2SO_4 solution. As shown in Fig. S6d, the C_{dl} value of AHGF-15 (1490 $\mu F/cm^2$) is significantly higher than that of AHGF-25 (984 $\mu F/cm^2$) and AHGF (164 $\mu F/cm^2$), greatly outperforming the traditional GF electrode [41]. Furthermore, as described in Table S1, BET analysis indicated that although the activation treatment only slightly increased the specific surface area of AHGF-15 and AHGF-25, the average pore diameter of AHGF-15 (5.86 nm) was significantly larger than that of AHGF (3.44 nm) and AHGF-25 (3.90 nm). This indicates that the significant improvement in the average pore diameter of AHGF-Y facilitates the diffusion of Br^- and the products, thereby enhancing its bromine extraction performance in the flow cell.

To determine the improved adsorption and capture ability of Br_2/Br^- within the modified AHGF, electrochemical performances were compared through single-cell tests. LSV tests were performed on AHGF and AHGF-Y at a scan rate of 10 mV/s within a potential range of 0.4–1.4 V to obtain the overpotential for bromine oxidation. Fig. 3a shows the LSV curves for each electrode, and water oxidation was not observed within the tested potential range. As shown in Fig. 3a, compared to AHGF and AHGF-25, AHGF-15 exhibited the lowest overpotential of 708 mV. These results indicate that the AHGF-15 sample has the best bromine evolution activity.

We plotted the Tafel curves to investigate the BrOR reaction kinetics of the three materials in greater depth (Fig. 3b). Theoretically, if the rate-limiting step of BrOR is Br^- electrolysis involving only a single electron transfer (producing bromine radical Br·), the Tafel slope should be 118 mV/dec (with $\alpha = 0.5$, $n = 0$) [42]. However, the Tafel slope of AHGF-15 is 78 mV/dec, significantly lower than that of AHGF-25 and AHGF, and notably lower than the theoretical value. This suggests that AHGF-15 may undergo additional steps that promote Br^- electrocatalytic oxidation before the rate-limiting step. The surface reaction kinetics of AHGF and AHGF-25 were limited, likely due to the effects of structure and surface

chemical composition on catalytic performance. Factors such as surface chemistry, structural morphology, conductivity, and charge accumulation could also influence the reaction rate. Through these analyses, we confirmed that AHGF-15 exhibited the best electrocatalytic activity for BrOR.

To gain a deeper understanding of the electrochemical behavior at the material-solution interface, we conducted EIS experiments (Fig. 3c and Fig. S7 in Supporting information). In the low-frequency region, the AHGF and AHGF-25 electrodes displayed nearly vertical lines, demonstrating good capacitive behavior at low frequencies. In the mid-frequency region, the Nyquist plots showed sloped curves known as Warburg resistance, which represents the frequency dependence of ion diffusion within the porous electrodes. The results showed that the EIS response of AHGF-15 exhibited two distinct response layers, in addition to the composite interfacial resistance of the substrate itself. This might be related to electronic conduction within the samples and the diffusion process of bromide ions (Br^-). Simultaneously, the impedance behavior of AHGF-25 and AHGF was similar, with a much larger arc radius in the Nyquist plots compared to AHGF-15. This indicated that the unique structure of AHGF-15 might contribute to faster electron transfer and more efficient bromide ion transport. Specifically, the AHGF-15 sample exhibited the best conductivity, superior electrochemical performance, shortened ion diffusion paths, and faster charge transfer, making it suitable for applications in electrochemical bromine extraction.

To further investigate the relationship between potential, structure and activity of electrode materials, we conducted *in-situ* EIS tests on the AHGF-15 sample. We compared the changes in charge transfer resistance and diffusion resistance at different potentials, and the specific Bode phase results were shown in Fig. 3d. In the high-frequency range (1 MHz to 10 kHz): The system was dominated by electrolyte resistance, and the phase change showed a weak correlation with the applied potential. In the mid-frequency range (10 kHz to 10 Hz), a larger phase angle was observed at lower potentials (0.933–1.033 V). This indicated an enhancement of interfacial charge transfer reactions in the system, possibly due to the occurrence of the bromine evolution reaction. In the low-frequency range (10 Hz to 0.1 Hz), the contact resistance between the electrode material and the electrolyte was reflected, which was related to the diffusion layer of Br^- on the surface of the carbon material electrode.

Through comparative electrochemical analyses of the samples, including LSV, Tafel and *in-situ* EIS, we verified the excellent electrocatalytic activity of AHGF-15 in the BrOR reaction. By optimizing the surface properties of the graphite felt and increasing the active sites, its ability for electrochemical bromine extraction could be further enhanced. These findings provide important insights for catalyst improvement and deepen our understanding of differences in material reactions.

At room temperature (25±3 °C), LSV tests were to determine the oxidation overpotential for bromine extraction [43,44]. Fig. 4a showed the LSV curves of the flow cell. The strong catalytic ability of AHGF-15 resulted in a lower onset voltage for bromine extraction. Although AHGF-25 also demonstrated some bromine extraction capability after 1.3 V, the rate and magnitude of the increase in current density were inferior to those of AHGF-15, indicating relatively weaker bromine extraction performance. Meanwhile, AHGF exhibited weak catalytic activity for Br^-, with no distinct onset voltage. The LSV results indicated that after CO_2 activation, the LSV onset potential of AHGF-Y shifted significantly forward compared to AHGF. This demonstrated that CO_2 activation enhanced the catalytic ability for bromide ion extraction. Among the samples, AHGF-15 exhibited the best bromine extraction capability, rapidly oxidizing bromine at a lower potential. Moreover, the LSV for dynamic bromine extraction of AHGF in Fig. 4a shows

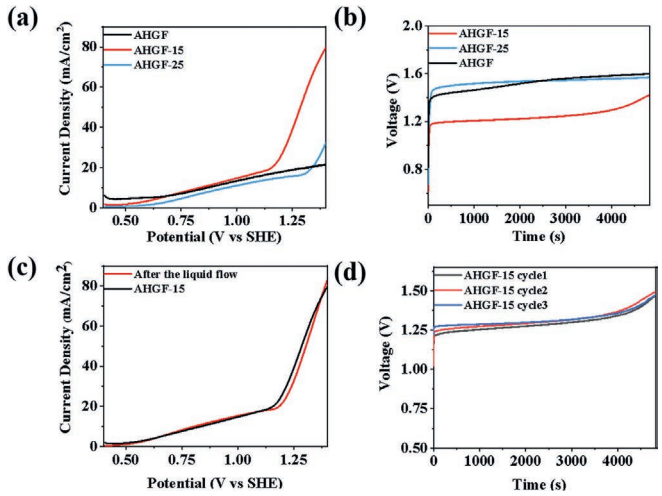


Fig. 4. (a) LSV curves of AHGF and AHGF-Y in the flow cell. (b) The constant current test of AHGF and AHGF-Y in the flow cell. (c) The LSV curves of AHGF-15 before and after the constant current test in the flow cell. (d) Three cycles of constant current bromine extraction with AHGF-15 in the flow cell.

a higher current density at 1.4 V compared to the static LSV in Fig. 3a, indicating that dynamic conditions are more favorable for mass transfer.

To evaluate the performances of the electrodes, bromine extraction yield and energy consumption are critical parameters. For AHGF and AHGF-Y, the parameters were calculated using the formulas derived from the data processing section of the supporting information. To confirm the bromine extraction performance of AHGF and AHGF-Y in flow cell, as shown in Table S2 (Supporting information), seven AHGF-Y samples with different CO_2 activation times worked as bromine electrodes. As shown in Fig. 4b, the voltage of AHGF-15 slowly increased to approximately 1.2 V and then gradually rose to nearly 1.4 V. This voltage was lower and more stable compared to AHGF and AHGF-25, suggesting a reduced likelihood of water oxidation side reactions for AHGF-15. Last, AHGF-15 exhibited the best catalytic performance for bromine extraction in flow cell, with nearly 94 % of bromide ions oxidized at an energy consumption of only 1.61 kJ/g. Thus, during the constant current test of 15 mA for bromine extraction in flow cells, AHGF-15 could effectively reduce the overpotential, enabling more bromide ions to participate in the redox reactions.

To gain further insight into the stability of active sites, the LSV curves of AHGF-15 before and after use in flow cell were compared. As shown in Fig. 4c, the onset potential of AHGF-15 after bromine extraction in the flow cell did not shift significantly, and the current density showed only a slight decrease. This indicates that AHGF-15 retained good activity and stability after the bromine extraction process. The XPS spectra in Figs. S8 and S9 (Supporting information) further confirmed the distribution of C and N elements in AHGF-15 after the flow reaction, showing that the forms of C and N remained nearly unchanged before and after the reaction. The improved electrode affinity addressed bromine oxidation issues and suppresses side reactions, resulting in enhanced bromine extraction performance and excellent durability. Therefore, the usage of the AHGF-15 negative electrode demonstrates superior performance and outstanding cycling stability. As shown in Fig. 4d, after three cycles, the bromine extraction performance of the AHGF-15 electrode remains stable.

In the flow system, bromine is generated on the negative electrode side. To enhance the value and efficiency of the system's overall products, the positive electrode side can be designed to produce equally valuable products. From the perspective of poten-

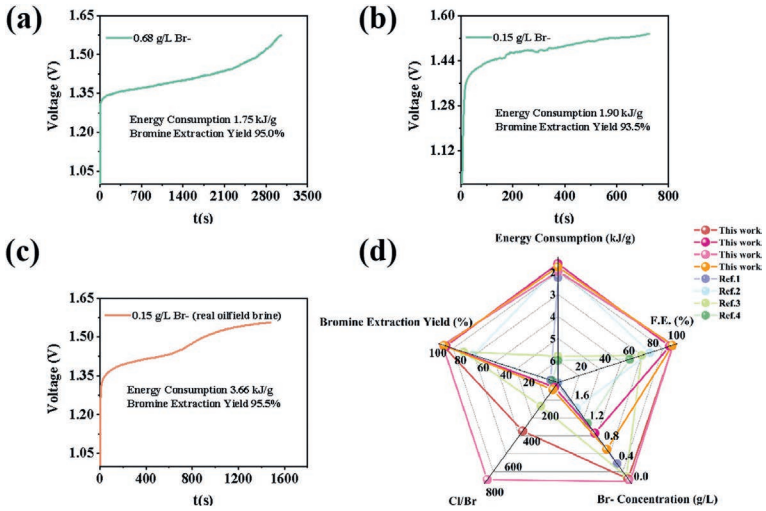


Fig. 5. Bromine extraction in flow system using AHGF-15 (a) in electrolyte with 0.68 g/L Br^- and 17 g/L Cl^-, (b) in electrolyte with 0.15 g/L Br^- and 17 g/L Cl^-, (c) in real oilfield brine containing 0.15 g/L Br^-. (d) Comparison of bromine extraction performance in this work with other representative electrodes in Table S6. Note: If the corresponding parameters are not mentioned in the literatures, they are considered as 0.

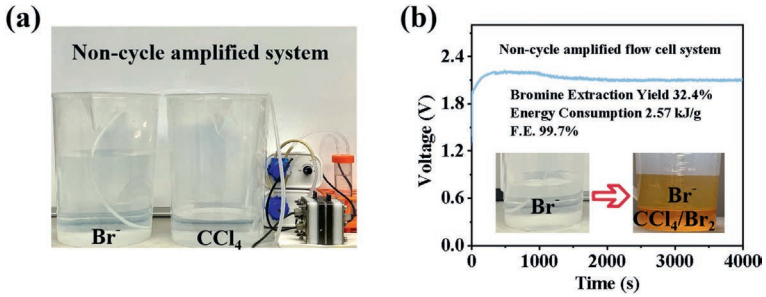


Fig. 6. (a) Non-cycle amplified system. (b) Bromine extraction in non-cycle amplified system using 1 g/L Br^- and 17 g/L Cl^-.

tial, carrying out the hydrogen evolution reaction (HER) on the positive electrode not only enables simultaneous bromine extraction and hydrogen production but also significantly improves the efficiency of electrical energy utilization. This approach presents an innovative strategy for combining bromine extraction with hydrogen generation, contributing to alleviating the energy shortage problem.

As shown in Fig. S10 and Table S3 (Supporting information), the selective bromine extraction can be successfully paired with HER in our flow cell. Using a flow circulation system in the negative electrode chamber, 83 mL of solution was processed at 100 mA for 1000 s. The bromine extraction yield reached 98.3 %, with energy consumption of only 1.81 kJ/mol. Meanwhile, hydrogen gas was co-produced at the positive electrode, yielding 12 mL, which was collected using the water displacement method. The hydrogen production is consistent with the theoretical hydrogen yield. This approach facilitates the effective use of electrical power, supplies bromine for industrial applications, and generates sustainable hydrogen energy.

The electrode was further applied to simulate the extraction of low-grade bromine resources. As shown in Fig. 5a and Table S4 (Supporting information), in a solution environment with 0.68 g/L Br^- and 17 g/L Cl^-, the bromine extraction yield of AHGF-15 could still reach 95.0 %, with energy consumption of only 1.75 kJ/g. Similarly, as shown in Fig. 5b, in an even lower concentration environment containing 0.15 g/L Br^- and 17 g/L Cl^-, the bromine extraction yield could maintain 93.5 %, with energy consumption slightly increased to 1.90 kJ/g. Additionally, as shown in Figs. S11 and S12 (Supporting information), even in environments with extremely low bromine ion concentrations of 100 mg/L and 50 mg/L, the electrode's bromine extraction efficiency can still reach 96.4 %, while maintaining low energy consumption. It is worth noting that the minimum concentration of bromine in seawater is currently 60 mg/L, which indicates that our device already possesses the capability to efficiently extract bromine from extremely low-concentration bromine resources, demonstrating its significant potential for practical applications. Table S4 summarizes the bromine extraction performance of AHGF-15 in flow systems using different electrolytes. Subsequently, as shown in Fig. 5c and Table S5 (Supporting information), the electrode was further applied to real oilfield brine containing 0.15 g/L Br^- and multiple interfering ions, such as SO_4^{2-}, NO_3^-, and Cl^-. In this system, AHGF-15 achieved a bromine extraction yield of 95.5 %, with an energy consumption of only 3.66 kJ/g, laying a solid foundation for its future practical application. Compared to other works (Fig. 5d and Table S6 in Supporting information), the flow bromine extraction system we constructed demonstrates advantages of high bromine extraction yield and low energy consumption in simulated electrolytes. Moreover, it also performed well in bromine extraction from raw underground brine. Ultimately, a good bromine extraction performance could be achieved, indicating its promising application potential and value for extracting bromine resources from low-grade brine. Additionally, as shown in Figs. 6a and b, in a non-cycle bromine extraction setup using a solution containing 1 g/L Br^- and 17 g/L Cl^-, 1 L of solution was processed, achieving a Faradaic efficiency of 99.7 %.

In this work, we proposed AHGF-Y based on mesoporous graphite felt fibers activated with CO_2. Such a simple and cost-effective approach could improve the structural and chemical prop-

erties. Performance tests were further conducted under flow conditions in bromine extraction, and it was found that due to the low ohmic resistance, enhanced conductivity, and better stability of AHGF-15, the bromine extraction yield reached nearly 94 % at an energy consumption of only 1.61 kJ/g in a flow cell with 1 g/L Br^-. In a low-grade system with 0.15 g/L Br^-, the bromine extraction yield was 93.5 %, with an energy consumption of just 1.90 kJ/g. Further application in real underground brine containing 0.15 g/L Br^- and a large number of Cl^- ions, as well as other interfering anions like $SO_4{}^2$- and $NO_3{}^-$, was conducted. The results demonstrated that AHGF-15 could still achieve bromine extraction yield of 95.5 % with an energy consumption of only 3.66 kJ/g. Additionally, in a non-cycle amplified bromine extraction setup, its Faradaic efficiency reached an near-unity of up to 99.7 %. In addition, selective bromine extraction was coupled with HER in the flow cell, achieving 98.3 % bromine extraction yield and 1.81 kJ/g energy consumption, where hydrogen gas was co-produced at the positive electrode. In conclusion, AHGF-Y demonstrated superior electrocatalytic performance in the bromine extraction flow cell developed in this work, exhibiting excellent bromine extraction yield and outstanding cycling stability.

CRediT authorship contribution statement

Ziyu Zhao: Writing – review & editing, Writing – original draft, Software, Methodology, Investigation, Formal analysis, Data curation. **Tianyue Qian:** Writing – review & editing, Supervision, Resources, Project administration, Funding acquisition, Formal analysis. **Changyu Yan:** Formal analysis, Data curation. **Xinhua He:** Formal analysis, Data curation. **Zhou Xu:** Validation, Investigation. **Wenjing Li:** Resources, Investigation. **Zhiling Xin:** Writing – review & editing, Supervision, Project administration, Funding acquisition. **Huifang Zhang:** Writing – review & editing, Supervision, Project administration, Funding acquisition. **Xuefeng Qian:** Writing – review & editing, Supervision, Resources, Project administration, Funding acquisition, Formal analysis, Conceptualization. **Jiantao Zai:** Writing – review & editing, Project administration, Funding acquisition, Formal analysis, Conceptualization.

Declaration of competing interest

The authors declare that they have no known competing financial interests or personal relationships that could have appeared to influence the work reported in this paper.

Acknowledgments

The work was supported by National Natural Science Foundation of China (Nos. 22461142137 and 22478242), Open Fund of Key Laboratory of Green and High-end Utilization of Salt Lake Resources (No. ISL2024-08) and Science and Technology Major Project of Shanghai.

Supplementary materials

Supplementary material associated with this article can be found, in the online version, at doi:10.1016/j.cclet.2025.111439.

References

[1] X. Zhang, X. Wang, J. Gao, et al., Chem. Eng. Process. 204 (2024) 109949.
[2] I. Cohen, B. Shapira, E. Avraham, et al., Environ. Sci. Technol. 52 (2018) 6275–6281.
[3] Q. Wang, J. Wang, G. Zhang, et al., R. Soc. Open Sci. 6 (2019) 191138.
[4] X. Zhang, Z. Ji, F. Liu, et al., Sep. Purif. Technol. 248 (2020) 117108.
[5] W. Zhang, S. Chai, X. Hao, et al., E3S Web Conf. 375 (2023) 03011.
[6] X. Zhang, W. Zhao, Y. Zhang, et al., Rev. Environ. Sci. Biotechnol. 20 (2021) 333–361.
[7] X. Yin, R. Li, W. Li, et al., Desalination 592 (2024) 118088.
[8] X. Zhou, Z. Ji, J. Wang, et al., J. Environ. Chem. Eng. 10 (2022) 107946.
[9] B. Sharkh, A. Al-Amoudi, M. Farooque, et al., NPJ Clean. Water 5 (2022) 1–16.
[10] W. Tu, Y. Zhao, W. Chan, et al., Water Res. 251 (2024) 121096.
[11] M. Suss, V. Presser, Joule 2 (2018) 10–15.
[12] M. Elimelech, M. Wilf, Science 333 (2011) 712–717.
[13] S. Porada, R. Zhao, A. Wal, et al., Prog. Mater. Sci. 58 (2013) 1388–1442.
[14] L. Tang, W. Lu, X. Li, et al., Energy Storage Mater. 70 (2024) 103532.
[15] M. Sun, G. Lowry, K. Gregory, Water Res. 47 (2013) 3723–3731.
[16] D. Desai, E. Beh, S. Sahu, et al., ACS Energy Lett. 3 (2018) 375–379.
[17] K. Ariyappan, P. Ragupathy, M. Ulaganathan, J. Electrochem. Soc. 168 (2021) 090566.
[18] C. Zhang, J. Ma, L. Wu, et al., Environ. Sci. Technol. 55 (2021) 4243–4267.
[19] X. Gao, A. Omosebi, J. Landon, et al., Energy Environ. Sci. 8 (2015) 897–909.
[20] Naresh, K. Satchidhanandam, K.R. Ilancheran, et al., J. Mater. Chem. A 12 (2024) 14669–14678.
[21] T. Le, M. Bechelany, M. Cretin, Carbon 122 (2017) 564–591.
[22] K. Kim, Y. Kim, J. Kim, et al., Mater. Chem. Phys. 131 (2011) 547–553.
[23] P. Yang, S. Dong, Y. Shu, et al., Molecules 29 (2024) 5015.
[24] K. Hatzell, M. Hatzell, K. Cook, et al., Environ. Sci. Technol. 49 (2015) 3040–3047.
[25] Y. Chang, J. Chen, D. Kabtamu, et al., J. Power Sources 364 (2017) 1–8.
[26] M. Montes-Morán, R. Young, Carbon 40 (2002) 857–875.
[27] C. Wang, Q. Lai, P. Xu, et al., Adv. Mater. 29 (2017) 1605815.
[28] X. Sun, D. Wang, H. Hu, et al., Trans. Tianjin Univ. 30 (2024) 74–89.
[29] M. Wu, R. Zhang, K. Liu, et al., J. Power Sources 442 (2019) 227255.
[30] J. Fu, L. Zhu, K. Jiang, et al., Chem. Eng. J. 415 (2021) 128982.
[31] C. Qiu, L. Jiang, Y. Gao, et al., Mater. Des. 230 (2023) 111952.
[32] R. Siegelman, E. Kim, J. Long, Nat. Mater. 20 (2021) 1060–1072.
[33] H. Li, M. Zhang, M. Wang, et al., ACS Sustain. Chem. Eng. 11 (2023) 7378–7387.
[34] H. Chen, J. Chen, D. Chen, et al., J. Mater. Sci. 54 (2019) 5625–5640.
[35] L. Feng, B. Yan, C. Wang, et al., Preparation of porous activated carbon materials and their application in supercapacitors, in: A. Uthaman, et al. (Eds.), Advanced Functional Porous Materials, Springer, Cham, 2022, pp. 587–612.
[36] T. Li, X. An, D. Fu, Energy Fuels 36 (2023) 191138.
[37] M. Boota, K. Hatzell, M. Beidaghi, et al., J. Electrochem. Soc. 161 (2014) A1078.
[38] G. Jeanmairet, B. Rotenberg, M. Salanne, et al., Chem. Rev. 122 (2022) 6456–6493.
[39] S. Vargheese, R. Kumar, Y. Haldorai, et al., Electrochemical double layer capacitors, in: S. Thomas, et al. (Eds.), Nanostructured Materials for Supercapacitors, Springer, Cham, 2022, pp. 27–52.
[40] V. Jadhav, R. Mane, P. Shinde, et al., Electrochemical supercapacitors: History, types, designing processes, operation mechanisms, and advantages and disadvantages, in: V. Jadhav, et al. (Eds.), Bismuth-Ferrite-Based Electrochemical Supercapacitors, Springer, Cham, 2020, pp. 11–36.
[41] Y. Zhang, A. Iqbal, J. Zai, et al., Org. Chem. Front. 9 (2022) 436–444.
[42] Y. Han, G. Su, J. Zhou, et al., J. Mater. Chem. A 10 (2022) 17652–17658.
[43] L. Dai, D.W. Chang, J.-B. Baek, et al., Small 8 (2012) 1130–1166.
[44] S. Ding, Q. Chen, S. Chen, et al., Chin. Chem. Lett. 34 (2023) 108232.